Patterning of the surface electrical potential on chalcogenide glasses by a thermo-electrical imprinting process

Ricardo Alvarado [a, ‡], *Lara Karam* [a, ‡], *Redouane Dahmani* [a], *Antoine Lepicard* [a], *Florian Calzavara*[b], *Andréa Piarristeguy*[c], *Annie Pradel*[c], *Thierry Cardinal* [b], *Fréderic Adamietz* [a], *Evelyne Fargin* [b], *Matthieu Chazot* [a, d], *Kathleen Richardson*[d], *Luc Vellutini*[a], *Marc Dussauze* [a]*

[a] Institut des Sciences Moléculaires, UMR 5255, Université de Bordeaux, 351 cours de la Libération, Talence Cedex 33405, France

[b] Institut de Chimie de la Matière Condensée de Bordeaux, Université de Bordeaux, 87 Avenue du Dr Schweitzer, Pessac F-33608,France

[c] Institut Charles Gerhardt Montpellier, UMR 5253 CNRS-UM-ENSCM, Université de Montpellier, Place E. Bataillon, Bât 15, cc 1503, 34095 Montpellier cedex 5 – France

[d] Department of Materials Science and Engineering, College of Optics and Photonics, University of Central Florida, Orlando, FL, United States

KEYWORDS:

Surface potential, Chalcogenide glasses, poling, glass structure

ABSTRACT

The development of novel sensing systems requires breakthroughs in the conception of multifunctional materials. In this sense, while extensive research has been dedicated to the individual tuning of the electrical or optical properties of different materials, the combination of both features would result in a promising field of research that would further extend opportunities for engineering novel function in sensor geometries. In the present work, we employed a highly attractive optical material for mid-infrared (MIR) sensing (chalcogenide glasses, ChG) and focused on the spatial control of its surface electrical potential via a thermoelectrical imprinting process. Different glass compositions based on the system Ge-Sb-S-Na were prepared by varying the sulfur stoichiometry and the sodium content. Each glass was thermally poled using electrodes with specific patterns, and subsequent structural modifications and surface electrical potential were then evaluated via Raman spectroscopy and Kelvin Probe Force Microscopy (KPFM). Raman cartographies show structural modifications attributed to alkali depletion following the patterns of the electrodes used for the imprinting process. Furthermore, KPFM measurements show clearly defined motifs on the electrical potential which are associated to charges implanted into the glass matrix. It was shown that the surface potential can vary in sign within an amplitude range of 10V and exhibit patterning at the micrometer scale. We observed that the efficiency of the surface

potential imprinted was dramatically impacted by the glass' sulfur and sodium content. Our results demonstrate for the first time the use of a one-step process, thermal poling, for large scale patterning of the surface potential of ChG creating a multi-functional material.

Introduction

In the context of lab-on-chip and other nanotechnological systems, control of a material's electrical functionality is a valuable lever that, if tunable, offers design flexibility to enhance device performance. The patterning of the electrical potential on the surface at micrometer or nanometer scale has been proven to be an effective strategy to assemble nanoparticles or nano-objects precisely at a desired location on a substrate through electrophoresis[1]. Xerography is a well-recognized technique that uses electrostatic forces to allow selective attachment of toner particles[2]. Since its early development, the technique has evolved considerably such that one can now talk about micro[3] or even nanoxerography[4–6]. The electrical patterning of the substrate, an appropriate charge carrier or electret, can be realized through atomic force microscopy[1,4,6], electron beam[7] or focused ion beam[8] with a lateral resolution of about a hundred nanometers. The main limitation of these techniques is that they are time

consuming when large areas (centimeter square) are considered. To circumvent this problem parallel printing processes to pattern charges on the electret over sizes approaching a centimeter square, during a single process cycle have been developed[3,5,9,10]. This stamp-like process doesn't deteriorate the resolution and even lower resolution (to 50 nm) can be obtained when a localized fringing field[10] is induced to direct the nanoparticle assembly. Guiding the growth of nano-objects on specific sites is not the only possibility that offers surface potential patterning. Rapid and reversible changes induced by potential to alter the focal length of liquid lenses has been achieved by tuning the electrochemical desorption of self-assembled monolayers (SAMs) onto a metal surface[11]. It is also possible to induce dynamic changes in interfacial properties such as wettability by generating conformational transitions of single layered amphiphilic molecules deposited onto a metallic substrate: a change in the sign of the potential leads to a transition between hydrophilic (molecules are straight) and hydrophobic (molecules are bent) nature of the surface[12].

Research efforts towards the development of components merging multiple functionalities are more and more essential. In this context, the combination of electrical

and optical functionalities on a single material represents a great benefit. Optical glasses such as chalcogenides (ChG) are particularly interesting for sensing applications, as they are transparent in the MIR, the spectral region in which the organic molecules fingerprint can be found. In this study, we demonstrate for the first time the patterning of the surface electrical potential of Ge-Sb-S-Na glasses via a one-step imprinting process covering large areas at once (centimeter square scale): thermal poling. This process consists in applying a DC field to a glass heated at moderate temperature; the glass is brought back to ambient temperature with the DC field still on. This freezes the electrical constraint at the surface of the glass and induces several other modifications: depletion of cations[13], structural rearrangements[14–16], modification of the surface reactivity[17–19], wettability change[20], surface potential[21], changes of the optical properties (modification of the index[22] and induced second order nonlinear response[23–27]) as well as the formation and patterning of glass-metal nanocomposites[28–31]. The patterning of these changes has been realized using structured electrodes that act like stamps to control the glass' surface properties leading to the design of functional elements such as linear[19] and nonlinear diffraction gratings[32] or arrays of micro-lenses[33]. In this study, we present evidence of the

viability in patterning of surface electrical potentials in glasses at the micrometer scale. Through parallel studies illustrating the influence of the glass' sodium and sulfur content on these surface properties combined with Raman microscopy, we proposed a mechanistic explanation as to the origin of the surface potential in order to generate effective and stable patterns for future applications.

Experimental Methods

Synthesis of ChG glasses: ChG glasses were prepared using high purity elemental Ge, Sb and S (Alfa Aesar, 99.999%). Anhydrous sodium sulfide (purity unspecified) was used to incorporate sodium as doping agent. Based on the stoichiometric composition $Ge_{25}Sb_{10}S_{65}$, different samples were prepared by varying either the S to Ge ratio (i.e. increasing the sulfur content) or by keeping the ratio between the other components constant and adding sodium. The nominal compositions of the different glasses are reported in table 1 as well as the name by which they will be referred to in the rest of the present work. Two series of glasses were synthetized: (i) A, B, C, D with constant sodium content to evidence the influence of sulfur and (ii) Na_0, Na_2, $Na_{5.5}$ with constant S to Ge ratio to discuss the influence of the sodium content. Raw materials were weighed out in a glove box under a nitrogen atmosphere before being inserted in a quartz ampule that was, then, put under vacuum (10^{-2} mbar) and sealed using an oxygen-methane torch. A rocking furnace was employed to ensure the homogeneity of the mixture. The temperature was increased at a rate of 1 °C min^{-1} up to 850 °C and left at this value for 12 h for homogenization. After this period of time, the rocking of the furnace was stopped and the temperature was set to gradually decrease to 750 °C (quenching temperature). The sample was then quenched in water and annealed for 6 h,

10 °C under its glass transition temperature (T_g); the T_g of the different glasses ranging between 250 and 350 °C. Finally, glasses were cut and polished into ~1 mm thick disks of 1 cm of diameter.

	Sample's name	Composition (at. %)				S/Ge ratio
		Ge	Sb	S	Na	
Influence of the S/Ge or sulfur content	A	24.5	10	64.5	**1**	**2.6**
	B	22	10	67	**1**	**3**
	C	20	10	69	**1**	**3.4**
	D	17	10	72	**1**	**4.2**
Influence of the sodium content	Na_0	22.5	10	67.5	**0**	**3**
	Na_2	22	9.8	66.2	**2**	**3**
	$Na_{5.5}$	21.3	9.4	64.8	**5.5**	**3**

Table 1: Atomic composition of the different glasses of interest and the name they are referred to.

Vibrational spectroscopy: Raman spectra were acquired using an XploRA PLUS (Horiba) spectrometer with a laser source at 785 nm focused on the sample via a 50x objective lens. Cartographies were acquired using a 100x (N.A. 0.9) objective lens on an area of 80 x 60 µm with a lateral resolution of ~2 µm.

Thermoelectrical imprinting: Electrical patterning was performed under a nitrogen atmosphere by pressing the ChG glass sample between two electrodes: a structured electrode used as a stamp located at the anode, and a silicon electrode at the cathode. A coverslip was used as a sacrificial layer in between the glass sample and the cathode. The structured electrode consists of a 100 nm thick Ti-Pt metallic films deposited on a silicate glass slide. The patterned electrode was prepared by a classical lithography process resulting in squared motifs (40x40 or 30x30 µm) leaving a 4 µm width electrically conductive Pt grid. The system was then heated to 210 °C, after reaching thermal stabilization, an electric field was applied at 375 $V.min^{-1}$ up to 0.9 kV. The temperature and DC

bias were kept constant for 30 min, then, the system was cooled down to room temperature before removal of the electric field.

Characterization of surface electrical potential: Measurements were performed at 100 nm from the surface by an AFM Dimensions Icon (Bruker) on PeakForce KPFM mode using a PFQNE-AL cantilever, over a 55 x 55 µm area and a resolution of 1024 points per line.

Results

Structural analysis of pristine glasses

Raman spectra of each pristine sample were acquired and normalized over their total integrated area **(Figure 1)**. Different models to describe GeS_2 glass networks have been proposed in the literature[34–37] resulting in different assignations for the characteristic Raman bands associated with this network.[38–40] A recent article regarding multimodal structural characterization of Ge-S-I[39] as well as previously reported DFT calculations[40] were used for the assignations in this work. The spectra presented in **Figure 1a** show different contributions associated with the stretching modes of Ge-S bonds in corner sharing (CS) GeS_4 tetrahedra[39,40] around 340 cm^{-1} and 415 cm^{-1} as well as Sb-S stretching modes in SbS_3 pyramids[41] resulting in a small shoulder around 300 cm^{-1}. The most striking variation when the amount of sulfur increases (i.e. going from glass A to D) is the apparition of new bands at 152 cm^{-1}, 219 cm^{-1} and 474 cm^{-1}, they correspond to S-S bonds.[39,42,43] The first two bands, present only when the sulfur content exceeds 70 at.%, are linked to the formation of sulfur rings (S_8) inside the glass matrix.[39,42] Another evolution when increasing the sulfur content, is the regular decrease of the contribution of the Ge related entities (340 and 415 cm^{-1}). This is consistent with the decrease of the Ge content in the composition when going from composition A to D. The Raman intensity of the modes related to Sb are not affected which is consistent with the fact the Sb content stays constant. More interestingly, the modes related to

either the Ge or Sb entities are observed at the same wavenumber, no frequency shift can be observed when the sulfur content increases. These observations suggest that the surplus of sulfur does not alter the glass forming units but rather the interconnections among them by establishing new homopolar S-S linkages. This results in the creation of S-S chains up to a given sulfur content (close to 70 at.%), passed this value, the increase of the sulfur content results in its organization into rings not linked to the other glass entities.

Let us focus on the effect of the sodium addition to the glass network (with fixed S to Ge ratio) on the basis of the Raman spectra presented in **Figure 1b**. Looking at the Raman response of samples Na_0 to $Na_{5.5}$, it appears that only slight changes can be observed when the sodium content varies from 0 to 5.5 at.%. In order to highlight these spectral variations, the difference Raman spectrum is presented in **Figure 1c**. It corresponds to the Raman spectrum of a sodium rich glass ($Na_{5.5}$) subtracted to the one of the glass without sodium (Na_0). Multiple contributions from GeS_4 tetrahedra can be observed (333, 375, 408 and 445 cm^{-1})[40]. The peaks at ~333 cm^{-1} and ~408 cm^{-1} can be ascribed to CS conformation[40] while the valleys at ~375 cm^{-1} and ~445 cm^{-1} are representative to an Edge Sharing (ES) arrangement[40]. The bands corresponding to the CS tetraedra appear positive in the Raman difference spectra (Na_0 minus $Na_{5.5}$) while those related to the ES are negative. This evolution denotes a modification of the interconnections of the germanate network with the addition of sodium as part of the CS tetrahedral units are substituted for the ES tetrahedra conformation. A peak at 304 cm^{-1} and a valley at around 264 cm^{-1} are present in the difference spectra and can be attributed to the contribution of antimony glass forming units. The addition of sodium in the vicinity of a SbS_3 pyramidal units can affect the strength of the Sb-S bonds. Therefore, the lower frequency of the band at 264 cm^{-1} for the sodium rich glasses ($Na_{5.5}$)

as compared to 304 cm^{-1} without sodium (Na_0) could be linked to weaker Sb-S bonds as part of the unit electronegativity is now distributed within the sodium coordination shell.

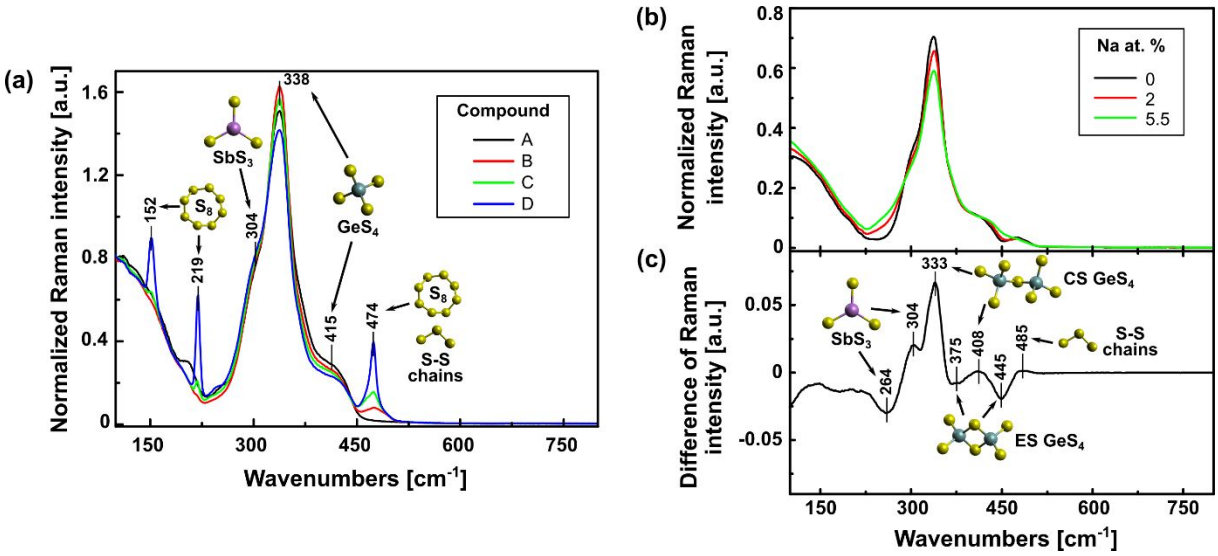


Figure 1. Raman spectra of the pristine ChG samples: (a) A, B, C and D glasses series with increasing S/Ge ratio, (b) Na_0, Na_2 and $Na_{5.5}$ glasses series with increasing sodium content and constant ratio between the other components and (c) Raman difference spectra: response of $Na_{5.5}$ subtracted to Na_0 response.

Spatial distribution of sodium after thermoelectrical imprinting

The thermally poled glasses were studied by Raman spectroscopy to evidence the structural variations induced by the process. Based on previous studies,[32,33] a spatial control of the sodium concentration through the use of a structured electrode is expected on the post-poling surface. In **Figure 2a**, are presented the Raman spectra from the post-poling surface of the A composition. The spectra were extracted from the regions that were *in contact* (IC) with the Ti-Pt metallic areas and *not in contact* (NC) with these conductive zones (i.e. middle of the squared patterns of the electrode). The variations between the two spectra are weak, thus, in order to highlight them, the Raman difference spectrum is presented **Figure 2b**. It corresponds to the spectrum extracted from

the NC region subtracted to the IC region. The resulting Raman difference spectrum closely matches the one presented in **Figure 1c** (Na_0 minus $Na_{5.5}$). Such similarity suggests in the IC zone the structure approaches the structure of a glass without sodium. This confirms the sodium depletion under the conductive zones of the electrode previously reported.[26] A similar methodology has been applied to the glasses presenting different S/Ge ratio (with same initial sodium content). The resulting spectra and Raman difference spectra are presented **Figure 3**. The ones of glass A have been reproduced for comparison with two different sulfur contents (glass samples B and D). All the Raman difference spectra show the same evolution. For all S to Ge ratio, thermal poling has the same effect: the post-poling glass in the IC zone shows a structure similar to a pristine glass without sodium. This shows the flexibility of the glass matrix which is rearranged through poling whatever the initial composition. **Figure 2c** are presented the Raman cartographies associated with selected bands of the Raman difference spectrum showing the spatial distribution of the structural rearrangements. The same pattern is observed for the distribution of all bands demonstrating the spatial coherence of the spectral variations. Furthermore, the pattern of the electrode can be recognized in these cartographies confirming that, through the use of a structured electrode, thermal poling can be successfully employed as an imprinting process. One should also notice that the imprinted patterns do not correspond exactly to the electrode design. This is due to a gradient in sodium concentration from the edge of the electrode toward the center of the non-conductive square. Such effect was accurately described in a study linked to the formation of gradient of refractive indices (GRIN) in similar glasses.[26]

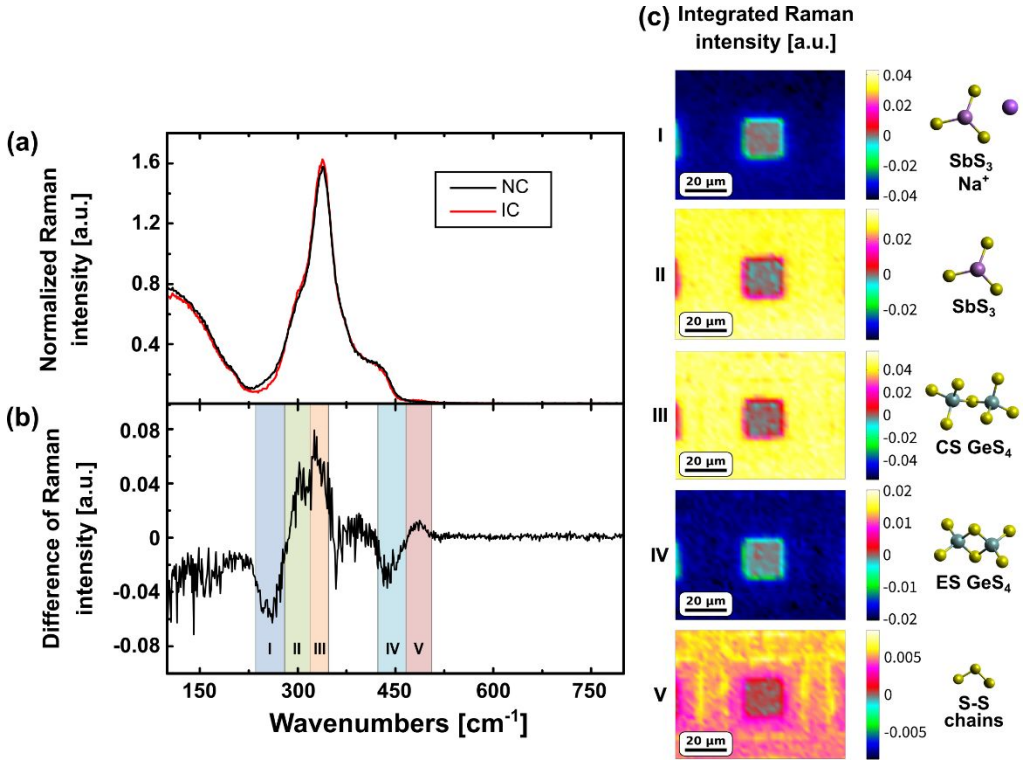


Figure 2. (a) Raman spectra from the thermally poled A glass, the black line corresponds to the region non in contact (NC) with the conductive zone and the red line in contact (IC). (b) Raman difference spectrum where the spectrum of the NC region has been subtracted to the IC region. (c) Spatial evolution of the Raman intensity of the different bands revealed by the Raman difference spectrum and the schematic representation of the glass units they are associated with.

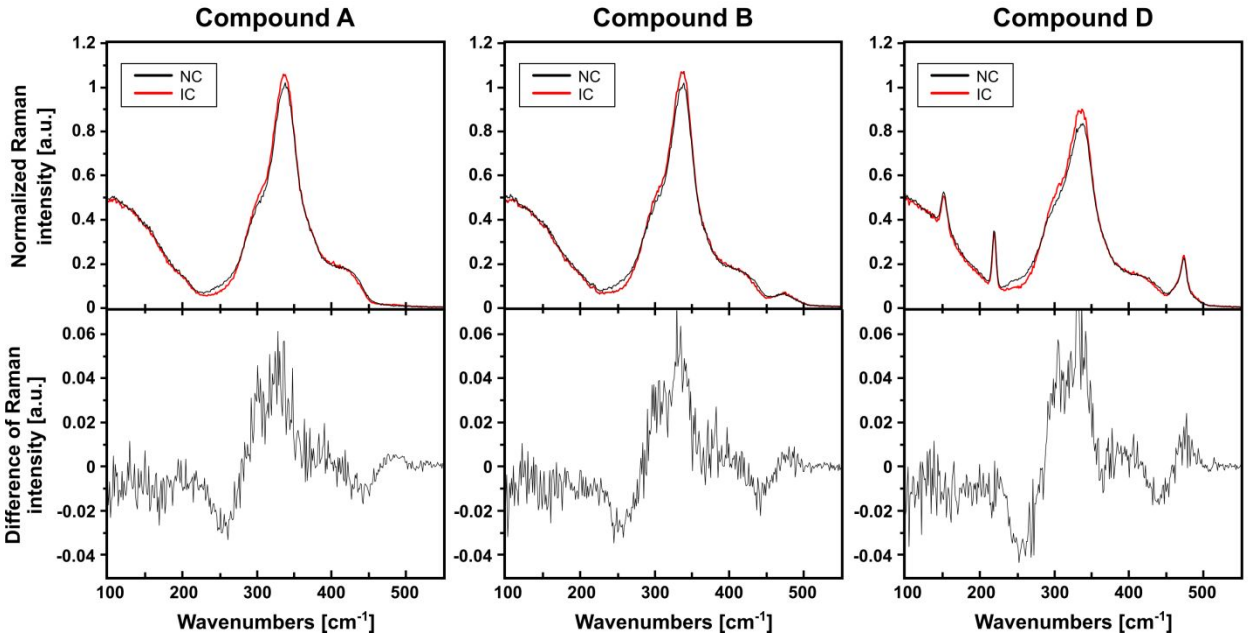


Figure 3. (Top) Raman spectra from the different thermally poled glasses A, B and D presenting different S/Ge ratio and same sodium content. The black lines correspond to the region not in contact (NC) with the conductive zone and the red line in contact (IC). (Bottom) Raman different spectra for each glass where the spectrum of the NC region has been subtracted from the spectrum of the IC region.

Patterning of the surface electrical potential

The post-poling topography as well as the resulting surface potential magnitude and spatial distribution for all the studied glasses are presented **Figure 4** and **Figure 5**. The **Figure 4** is dedicated to the influence of the sulfur content with the series of glasses A, B, C and D (1 at. % of sodium) while in **Figure 5** the emphasis is put on the sodium content with the Na_0, Na_2 and $Na_{5.5}$ glasses.

Let us focus first on the **Figure 4** with the A, B, C and D glasses. Topography variations of a maximum of 50 nm amplitude can be observed. The main changes are located at the edges of the

electrode; the rest of the surface is rather flat for all samples with even smaller changes as the sulfur content increases. Looking at the surface potential of the poled A glass sample, one can clearly recognize the pattern of the electrode resulting in negatively charged regions when IC with the electrode and positively charged regions when NC. The region IC, as the Raman study has shown, corresponds to a sodium-depleted region. The amplitude variation of surface potential is 9 V for this sample. Glass B only shows an amplitude variation of 1 V and ~0.2-0.4 V for C and D. Based on this observation the bigger the ratio S to Ge is (i.e. the more sulfur in the matrix), the lower the magnitude of the potential is: it is maximal for glass A (stoichiometric composition) and diminishes in B until the pattern can barely be observed for glasses C and D.

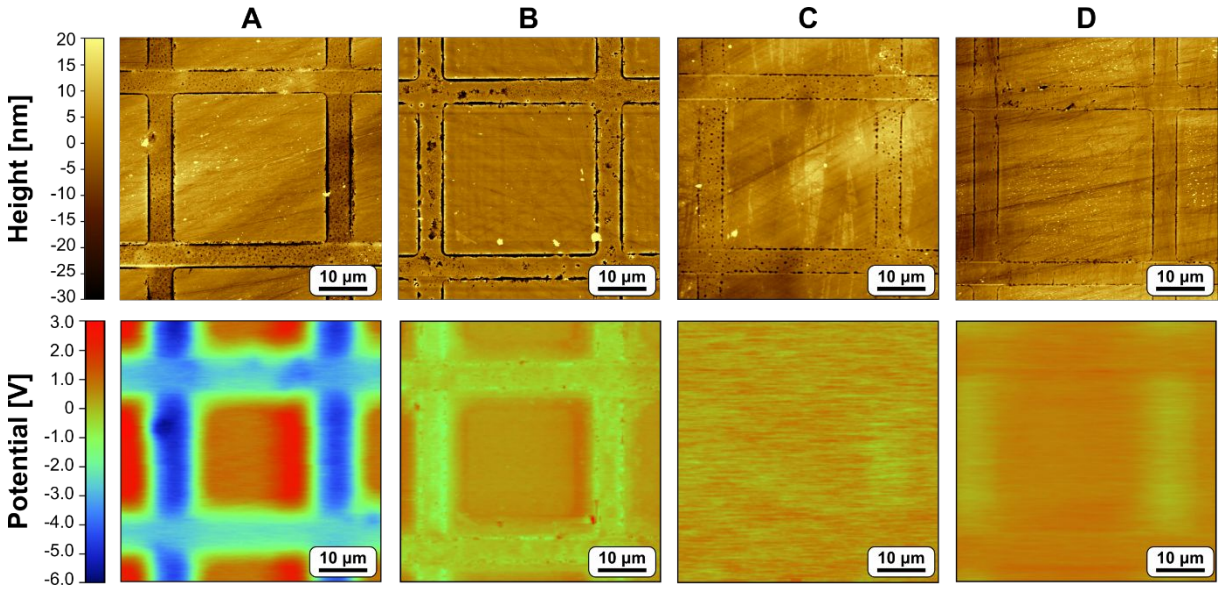


Figure 4. AFM measured topography (top) and KPFM measured surface potential (bottom) images of the post-poling surface of glasses A, B, C and D i.e. increasing sulfur content with fixed sodium content.

Regarding the influence of the sodium content the first comment we have to make is that when no sodium is present in the initial composition (Na_0), the post-poling surface does not present any

topographic variation and no potential structuring is observed. For this reason, the measurements concerning this composition are not presented here. In Figure 5, can be found the post-poling topography and surface potential of glasses with higher sodium contents (Na_2 and $Na_{5.5}$). It appears that, for the imprinting process to be successful, the presence of alkali in the initial composition is necessary. Increasing the initial sodium content results in variation of the topography, the more the initial sodium content increases the stronger the topography changes are. The surface potential structuring can be observed for Na_2 but with higher sodium contents ($Na_{5.5}$), it tends to disappear.

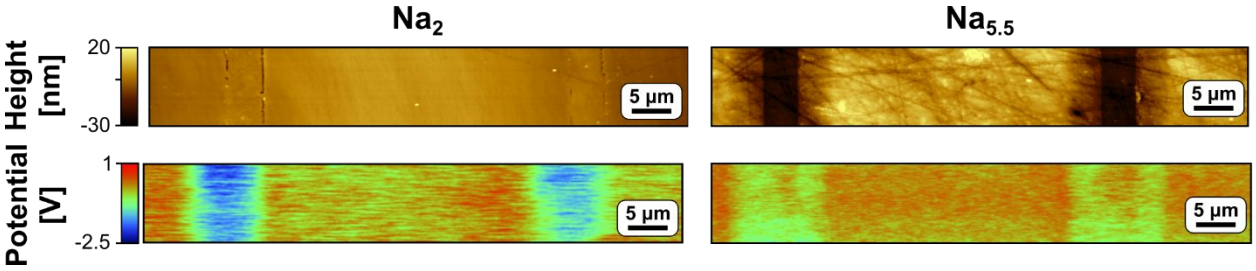


Figure 5. AFM measured topography (top) and KPFM measured surface potential (bottom) images of the post-poling surface of glasses Na_2 and $Na_{5.5}$ i.e. increasing sodium content with other component's ratios constant. The results obtained for Na_0 (no sodium) are not presented as no effect – topology or potential – were observed in the absence of alkali cation in the initial composition.

Discussion

The main objective of this study is to engineer a spatially varying and stable surface electrical potential on a glass optical materials that could open new opportunities in the development of multifunctional approach in inorganic glass science. Charge implantation has been successfully realized in chalcogenide materials since the 70's with the development of xerography processes notably on amorphous selenium.[44,45] These works have demonstrated the potential of chalcogenide materials to sustain electrical or plasma processes for the fabrication of charged surfaces.

Nevertheless, in our case, the multifunctional properties targeted require novel objectives in terms of long term stability and micrometric spatial control. As compared to a xerography approach, the thermo-electrical imprinting process is considerably different because of the nature of the charge carriers as it involves necessarily alkali cations. The Raman mapping reported has evidenced the ability of this thermo-electrical process to control the sodium spatial distribution within the chalcogenide glassy matrix at the micrometer scale for all the glass compositions studied. This structural study also points out the similarity observed between spectral variations from glasses prepared with and without sodium addition (Figure 1) and the ones measured when the sodium is depleted from the glass matrix under the electrical constrain (Figure 2). It shows the flexibility of the glass network and its ability to rearrange under a high electric field at temperatures below its glass transition. Regarding the objective of surface electrical potential patterning, the presented results have also demonstrated that by using this imprinting poling process, stable surface charges can only be obtained with sodium doped glasses which denotes the importance of cationic charge carriers to modify the surface electrical properties for these germanate chalcogenide glasses.

To analyze the surface potential patterned for this series of glasses, one should consider the respective effects of: (i) the location of the trapped charges which have to be promoted close to the surface in order to influence the surface potential and (ii) the energy level of the traps which will determine the stability of the induced surface potential.

Concerning charged surface stabilities, let's remind that research studies in the domains of polarized or charged materials have demonstrated the importance of a material disorder state to enable a slow discharge[46–50]. Depending on the trap energy distribution, charges can diffuse to reach a "sink" to be neutralized as described in a classical trapping model developed to describe electronic relaxation in amorphous semiconductors[46,51]. In addition, in reference to works done on

the photosensitivity or on thermal poling of chalcogenide glasses, it was shown that structural rearrangements induced by the optical or electrical polarization treatments are very favorable for the stability of charges as the modified structure considerably increases the energy barrier of the traps[52,53].

To summarize the results of this study: (i) we have observed that the surface potential patterning is efficient only for the composition stoichiometric in sulfur, and (ii) if the sodium content increases, the electrical potential values decrease together with an enhancement of the surface topology variations. Both findings denote the importance of the glass local structure to achieve the targeted functional properties.

Concerning the effect of the sulfur content, it is not possible to conclude if the absence of surface potential observed for the rich-sulfur glasses can be linked to an implantation of trapped charges preferentially localized in the bulk or if it can be linked to a very poor stability of charges at the surface. Nevertheless, the structural study has confirmed a significant amount of S-S homopolar bonds and the presence of sulfur rings in the glassy structure, it induces a real change in the local homogeneity and polarizability of the structure which necessarily affect the distribution of trap energies and as a consequence the local transport/diffusion of charges. Under this assumption, one may expect an easier transport of the charge carriers in the poled matrix with the increase of homopolar bonds which could locally facilitate an electronic transport in the amorphous structure. In any case, it denotes the key role of the glass local molecular structure to promote stable surface charges.

Focusing our analysis on the influence of the sodium content in the glass matrix, one should point out that when the amount of alkali increase the imprinting process induces non negligible surface topology variations (steps of 50 nm for 5.5 mol% of Na). This surface relief modification

is expected from previous studies on poled ionic glasses[54]. It denotes the presence of matter displacement, volume contraction and glass density variations induced during the alkali-depleted layer formation. In such a case, we can note a clear decrease of the patterned surface potential amplitude when the amount of charge carriers involved increase imposing large modification of the physico-chemical properties of the glassy material surface.

Furthermore, one should evoke the spatial control of charge implantation managed by this imprinting process. In regards to a future electrical/optical multifunctional approach, a spatial control of the surface potential at the micrometer scale is essential in order to suite with the sizes of photonic waveguides for example. This study has demonstrated the potential of this polarization process to achieve such objectives. To explain the surface potential patterns obtained, one should focus on the electrode configuration. : a juxtaposition of conductive and non-conductive zones (as used in this study with a metallic thin film patterned by a lithography method). Such a juxtaposition of conductive and non-conductive area allows to promote in plane field components which can promote and control surface current direction. Such effect was recently reported for the electro-optical second harmonic generation response obtained for a similar glass system[32]. These surface currents controlled by the electrode geometry might be at the origin of the sign control of the surface potential which allow accurate patterning at the micrometric scale, yet further studies will be required to explain this process in detail.

Finally, the question of the stability of the induced patterned surface potential with time is crucial for further integration in multifunctional systems. This temporal aspect wasn't the main objective of this work, however to justify the real interest of these polarized surfaces, is presented in figure 6 the surface potential measured on a sample right after the thermoelectrical treatment and 24 months later. The electrode used is constituted of a circular pattern. One can observe that, if the

amplitude variation of surface potential has significantly decreased (from 3 V to 1.6 V), the patterning of the surface potential is retained after two years. These preliminary results on the stability of the poled chalcogenide surface properties are encouraging. Some additional characterizations are actually in progress.

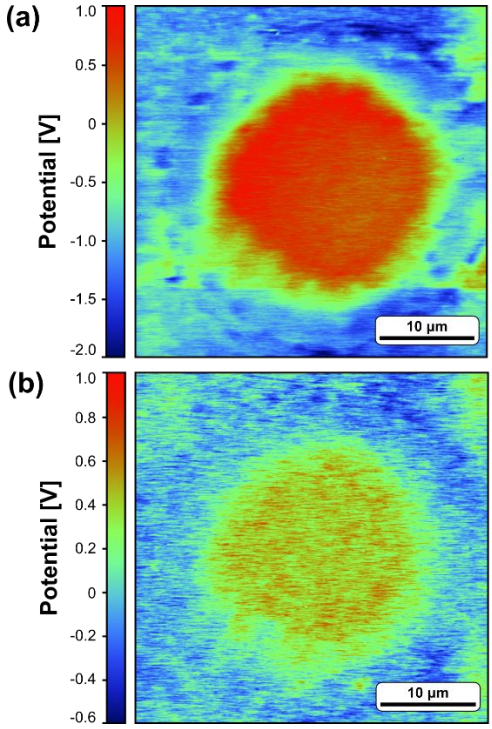


Figure 6. KPFM imaging of a ChG sample after thermal poling at after being poled (a) and after 24 months of being poled (b).

Conclusions

A spatial control of the surface electrical potential of chalcogenide glasses in the system Ge-Sb-S-Na was achieved using a thermo-electrical imprinting process. The charged chalcogenide surfaces have shown electrical potentials varying in sign within an amplitude range of 10V. The induced patterns can be accurate at the micrometer scale and effective on large centimeter scales. Combining data from structural characterization and Kelvin Probe Force Microscopy (KPFM), the

glass composition has been found to play a crucial role on the final electrical properties. The presence of S-S homopolar bonds and sulfur rings in glasses as well as the sodium content largely influence the induced surface potential. Such set of results open the way to create new multi-functional (optical and electrical) surfaces.

AUTHOR INFORMATION

Corresponding Author

* E-mail: marc.dussauze@u-bordeaux.fr

Author Contributions

The manuscript was written through contributions of all authors. All authors have given approval to the final version of the manuscript. ‡These authors contributed equally.

Acknowledgment

The authors gratefully acknowledge the financial support of: IdEx Bordeaux (Cluster of Excellence LAPHIA and the allocated grant referred to as ANR-10-IDEX-03-03) and the CNRS project EMERGENCE @INC2019. This project has received funding from the European Union's Horizon 202 research program under the Marie Skłodowska-Curie grant agreement No 823941 (FUNGLASS).

REFERENCES

(1) Mesquida, P.; Stemmer, A. Attaching Silica Nanoparticles from Suspension onto Surface Charge Patterns Generated by a Conductive Atomic Force Microscope Tip. *Adv. Mater.* **2001**, *13* (18), 1395–1398. https://doi.org/10.1002/1521-4095(200109)13:18<1395::AID-ADMA1395>3.0.CO;2-0.

(2) Schaffert, R. M.; Oughton, C. D. Xerography: A New Principle of Photography and Graphic Reproduction. *J. Opt. Soc. Am.* **1948**, *38* (12), 991. https://doi.org/10.1364/JOSA.38.000991.

(3) Jacobs, H. O. Submicrometer Patterning of Charge in Thin-Film Electrets. *Science* **2001**, *291* (5509), 1763–1766. https://doi.org/10.1126/science.1057061.

(4) Palleau, E.; Sangeetha, N. M.; Viau, G.; Marty, J.-D.; Ressier, L. Coulomb Force Directed Single and Binary Assembly of Nanoparticles from Aqueous Dispersions by AFM Nanoxerography. *ACS Nano* **2011**, *5* (5), 4228–4235. https://doi.org/10.1021/nn2011893.

(5) Jacobs, H. O.; Campbell, S. A.; Steward, M. G. Approaching Nanoxerography: The Use of Electrostatic Forces to Position Nanoparticles with 100 Nm Scale Resolution. *Adv. Mater.* **2002**, *14* (21), 1553–1557. https://doi.org/10.1002/1521-4095(20021104)14:21<1553::AID-ADMA1553>3.0.CO;2-9.

(6) Ressier, L.; Palleau, E.; Garcia, C.; Viau, G.; Viallet, B. How to Control AFM Nanoxerography for the Templated Monolayered Assembly of 2 Nm Colloidal Gold Nanoparticles. *IEEE Trans. Nanotechnol.* **2009**, *8* (4), 487–491. https://doi.org/10.1109/TNANO.2009.2016089.

(7) Fudouzi, H.; Kobayashi, M.; Shinya>, N. Assembling 100 Nm Scale Particles by an Electrostatic Potential Field. *J. Nanoparticle Res.* **2001**, *3* (2/3), 193–200. https://doi.org/10.1023/A:1017903123384.

(8) Fudouzi, H.; Kobayashi, M.; Shinya, N. Site-Controlled Deposition of Microsized Particles Using an Electrostatic Assembly. *Adv. Mater.* **2002**, *14* (22), 1649–1652. https://doi.org/10.1002/1521-4095(20021118)14:22<1649::AID-ADMA1649>3.0.CO;2-Z.

(9) Ma, X.; Zhao, D.; Xue, M.; Wang, H.; Cao, T. Selective Discharge of Electrostatic Charges on Electrets Using a Patterned Hydrogel Stamp. *Angew. Chem. Int. Ed.* **2010**, *49* (32), 5537–5540. https://doi.org/10.1002/anie.201000766.

(10) Barry, C. R.; Jacobs, H. O. Fringing Field Directed Assembly of Nanomaterials. *Nano Lett.* **2006**, *6* (12), 2790–2796. https://doi.org/10.1021/nl0618703.

(11) Gorman, C. B.; Biebuyck, H. A.; Whitesides, G. M. Control of the Shape of Liquid Lenses on a Modified Gold Surface Using an Applied Electrical Potential across a

Self-Assembled Monolayer. *Langmuir* **1995**, *11* (6), 2242–2246. https://doi.org/10.1021/la00006a063.

(12) Lahann, J. A Reversibly Switching Surface. *Science* **2003**, *299* (5605), 371–374. https://doi.org/10.1126/science.1078933.

(13) Dussauze, M.; Fargin, E.; Lahaye, M.; Rodriguez, V.; Adamietz, F. Large Second-Harmonic Generation of Thermally Poled Sodium Borophosphate Glasses. *Opt. Express* **2005**, *13* (11), 4064–4069.

(14) Dussauze, M.; Kamitsos, E. I.; Fargin, E.; Rodriguez, V. Structural Rearrangements and Second-Order Optical Response in the Space Charge Layer of Thermally Poled Sodium−Niobium Borophosphate Glasses. *J. Phys. Chem. C* **2007**, *111* (39), 14560–14566. https://doi.org/10.1021/jp074335f.

(15) Dussauze, M.; Rodriguez, V.; Lipovskii, A.; Petrov, M.; Smith, C.; Richardson, K.; Cardinal, T.; Fargin, E.; Kamitsos, E. I. How Does Thermal Poling Affect the Structure of Soda-Lime Glass? *J. Phys. Chem. C* **2010**, *114* (29), 12754–12759. https://doi.org/10.1021/jp1033905.

(16) Redkov, A. V.; Melehin, V. G.; Lipovskii, A. A. How Does Thermal Poling Produce Interstitial Molecular Oxygen in Silicate Glasses? *J. Phys. Chem. C* **2015**, *119* (30), 17298–17307. https://doi.org/10.1021/acs.jpcc.5b04513.

(17) Lepicard, A.; Cardinal, T.; Fargin, E.; Adamietz, F.; Rodriguez, V.; Richardson, K.; Dussauze, M. Surface Reactivity Control of a Borosilicate Glass Using Thermal Poling. *J. Phys. Chem. C* **2015**, *119* (40), 22999–23007. https://doi.org/10.1021/acs.jpcc.5b07139.

(18) Lepicard, A.; Cardinal, T.; Fargin, E.; Adamietz, F.; Rodriguez, V.; Richardson, K.; Dussauze, M. Micro-Structuring the Surface Reactivity of a Borosilicate Glass via Thermal Poling. *Chem. Phys. Lett.* **2016**, *664*, 10–15. https://doi.org/10.1016/j.cplett.2016.09.077.

(19) Kamenskii, A. N.; Reduto, I. V.; Petrikov, V. D.; Lipovskii, A. A. Effective Diffraction Gratings via Acidic Etching of Thermally Poled Glass. *Opt. Mater.* **2016**, *62*, 250–254. https://doi.org/10.1016/j.optmat.2016.09.074.

(20) Lind, F.; Palles, D.; Möncke, D.; Kamitsos, E. I.; Wondraczek, L. Modifying the Surface Wetting Behavior of Soda-Lime Silicate Glass Substrates through Thermal

Poling. *J. Non-Cryst. Solids* **2017**, *462*, 47–50. https://doi.org/10.1016/j.jnoncrysol.2017.02.006.

(21) Yudistira, D.; Faccio, D.; Corbari, C.; Kazansky, P. G.; Benchabane, S.; Pruneri, V. Electric Surface Potential and Frozen-in Field Direct Measurements in Thermally Poled Silica. *Appl. Phys. Lett.* **2008**, *92* (1), 012912. https://doi.org/10.1063/1.2827175.

(22) Dussauze, M.; Kamitsos, E. I.; Fargin, E.; Rodriguez, V. Refractive Index Distribution in the Non-Linear Optical Layer of Thermally Poled Oxide Glasses. *Chem. Phys. Lett.* **2009**, *470* (1–3), 63–66. https://doi.org/10.1016/j.cplett.2009.01.007.

(23) Myers, R. A.; Mukherjee, N.; Brueck, S. R. Large Second-Order Nonlinearity in Poled Fused Silica. *Opt. Lett.* **1991**, *16* (22), 1732–1734.

(24) Quiquempois, Y.; Godbout, N.; Lacroix, S. Model of Charge Migration during Thermal Poling in Silica Glasses: Evidence of a Voltage Threshold for the Onset of a Second-Order Nonlinearity. *Phys. Rev. A* **2002**, *65* (4). https://doi.org/10.1103/PhysRevA.65.043816.

(25) Dussauze, M.; Cremoux, T.; Adamietz, F.; Rodriguez, V.; Fargin, E.; Yang, G.; Cardinal, T. Thermal Poling of Optical Glasses: Mechanisms and Second-Order Optical Properties. *Int. J. Appl. Glass Sci.* **2012**, *3* (4), 309–320. https://doi.org/10.1111/ijag.12001.

(26) Dussauze, M.; Malakho, A.; Fargin, E.; Manaud, J. P.; Rodriguez, V.; Adamietz, F.; Lazoryak, B. Large Second Order Optical Nonlinearity in Thermally Poled Amorphous Niobium Borophosphate Films. *J. Appl. Phys.* **2006**, *100* (1), 013108. https://doi.org/10.1063/1.2210572.

(27) Karam, L.; Adamietz, F.; Michau, D.; Gonçalves, C.; Kang, M.; Sharma, R.; Murugan, G. S.; Cardinal, T.; Fargin, E.; Rodriguez, V.; Richardson, K. A.; Dussauze, M. Electrically Micro-Polarized Amorphous Sodo-Niobate Film Competing with Crystalline Lithium Niobate Second-Order Optical Response. *Adv. Opt. Mater.* **2020**, 2000202. https://doi.org/10.1002/adom.202000202.

(28) Deparis, O.; Kazansky, P. G.; Abdolvand, A.; Podlipensky, A.; Seifert, G.; Graener, H. Poling-Assisted Bleaching of Metal-Doped Nanocomposite Glass. *Appl. Phys. Lett.* **2004**, *85* (6), 872–874. https://doi.org/10.1063/1.1779966.

(29) Beresna, M.; Kazansky, P. G.; Deparis, O.; Carvalho, I. C. S.; Takahashi, S.; Zayats, A. V. Poling-Assisted Fabrication of Plasmonic Nanocomposite Devices in Glass. *Adv. Mater.* **2010**, *22* (39), 4368–4372. https://doi.org/10.1002/adma.201001222.

(30) Brunkov, P. N.; Melekhin, V. G.; Goncharov, V. V.; Lipovskii, A. A.; Petrov, M. I. Submicron-Resolved Relief Formation in Poled Glasses and Glass-Metal Nanocomposites. *Tech. Phys. Lett.* **2008**, *34* (12), 1030–1033. https://doi.org/10.1134/S1063785008120122.

(31) Chervinskii, S.; Sevriuk, V.; Reduto, I.; Lipovskii, A. Formation and 2D-Patterning of Silver Nanoisland Film Using Thermal Poling and out-Diffusion from Glass. *J. Appl. Phys.* **2013**, *114* (22), 224301. https://doi.org/10.1063/1.4840996.

(32) Lepicard, A.; Adamietz, F.; Rodriguez, V.; Richardson, K.; Dussauze, M. Demonstration of Dimensional Control and Stabilization of Second Harmonic Electro-Optical Response in Chalcogenide Glasses. *Opt. Mater. Express* **2018**, *8* (6), 1613. https://doi.org/10.1364/OME.8.001613.

(33) Lepicard, A.; Bondu, F.; Kang, M.; Sisken, L.; Yadav, A.; Adamietz, F.; Rodriguez, V.; Richardson, K.; Dussauze, M. Long-Lived Monolithic Micro-Optics for Multispectral GRIN Applications. *Sci. Rep.* **2018**, *8* (1), 7388. https://doi.org/10.1038/s41598-018-25481-x.

(34) Griffiths, J. E.; Phillips, J. C.; Espinosa, G. P.; Remeika, J. P.; Bridenbaugh, P. M. Assignment of the Companion A1c Line in GeX(S, Se)$_{1-x}$ Glasses. *Phys. Status Solidi B* **1984**, *122* (1), K11–K15. https://doi.org/10.1002/pssb.2221220148.

(35) Bridenbaugh, P. M.; Espinosa, G. P.; Griffiths, J. E.; Phillips, J. C.; Remeika, J. P. Microscopic Origin of the Companion A 1 Raman Line in Glassy Ge (S, Se)$_2$. *Phys. Rev. B* **1979**, *20* (10), 4140–4144. https://doi.org/10.1103/PhysRevB.20.4140.

(36) Kawamoto, Y.; Kawashima, C. Infrared and Raman Spectroscopic Studies on Short-Range Structure of Vitreous GeS_2. *Mater. Res. Bull.* **1982**, *17* (12), 1511–1516. https://doi.org/10.1016/0025-5408(82)90206-9.

(37) Jackson, K.; Briley, A.; Grossman, S.; Porezag, D. V.; Pederson, M. R. Raman-Active Modes of a − $GeSe_2$ and a − GeS_2 : A First-Principles Study. *Phys. Rev. B* **1999**, *60* (22), R14985–R14989. https://doi.org/10.1103/PhysRevB.60.R14985.

(38) Bérubé, J. P.; Messaddeq, S. H.; Bernier, M.; Skripachev, I.; Messaddeq, Y.; Vallée, R. Tailoring the Refractive Index of Ge-S Based Glass for 3D Embedded Waveguides Operating in the Mid-IR Region. *Opt. Express* **2014**, *22* (21), 26103. https://doi.org/10.1364/OE.22.026103.

(39) Chazot, M.; Mereau, R.; El Amraoui, M.; Adamietz, F.; Messaddeq, Y.; Rodriguez, V. Multimodal Structural Characterization of Ge–S–I Glasses by Combination of DFT Calculation and IR and Polarized Raman Spectroscopy. *J. Phys. Chem. C* **2019**, *123* (6), 3758–3769. https://doi.org/10.1021/acs.jpcc.8b11187.

(40) Masselin, P.; Le Coq, D.; Cuisset, A.; Bychkov, E. Spatially Resolved Raman Analysis of Laser Induced Refractive Index Variation in Chalcogenide Glass. *Opt. Mater. Express* **2012**, *2* (12), 1768. https://doi.org/10.1364/OME.2.001768.

(41) Koudelka, L.; Frumar, M.; Pisárčik, M. Raman Spectra of Ge-Sb-S System Glasses in the S-Rich Region. *J. Non-Cryst. Solids* **1980**, *41* (2), 171–178. https://doi.org/10.1016/0022-3093(80)90162-3.

(42) Susarla, S.; Tsafack, T.; Owuor, P. S.; Puthirath, A. B.; Hachtel, J. A.; Babu, G.; Apte, A.; Jawdat, B. I.; Hilario, M. S.; Lerma, A.; et al. High-K Dielectric Sulfur-Selenium Alloys. *Sci. Adv.* **2019**, *5* (5), eaau9785. https://doi.org/10.1126/sciadv.aau9785.

(43) Ward, A. T. Raman Spectroscopy of Sulfur, Sulfur-Selenium, and Sulfur-Arsenic Mixtures. *J. Phys. Chem.* **1968**, *72* (12), 4133–4139. https://doi.org/10.1021/j100858a031.

(44) Pfister, G. Electronic Properties of Chalcogenide Glasses and Their Use in Xerography. *J. Electron. Mater.* **1979**, *8* (6), 789–837. https://doi.org/10.1007/BF02651186.

(45) Mikla, V. I.; Mikla, V. V. Xerographic Spectroscopy of Gap States in Se-Rich Amorphous Semiconductors Review. *J. Non-Cryst. Solids* **2011**, *357* (22–23), 3675–3688. https://doi.org/10.1016/j.jnoncrysol.2011.07.018.

(46) Pfister, G.; Scher, H. Dispersive (Non-Gaussian) Transient Transport in Disordered Solids. *Adv. Phys.* **1978**, *27* (5), 747–798. https://doi.org/10.1080/00018737800101474.

(47) Yuan, N.; Li, J. SiO_2 Film Electret with High Surface Potential Stability. *Appl. Surf. Sci.* **2005**, *252* (2), 455–460. https://doi.org/10.1016/j.apsusc.2005.01.025.

(48) Andriesh, A. M.; Buzdugan, A. I.; Zelenina, L. I.; Shutov, S. D. Dark Decay of Surface Potential in Vitreous As_2S_3. *Phys. Status Solidi A* **1982**, *74* (1), K79–K82. https://doi.org/10.1002/pssa.2210740161.

(49) Schnörer, H.; Haarer, D.; Blumen, A. Crossover from Dispersive to Nondispersive Transport in a Trap-Controlled Hopping Model. *Phys. Rev. B* **1988**, *38* (12), 8097–8101. https://doi.org/10.1103/PhysRevB.38.8097.

(50) Godzik, K.; Schirmacher, W. Theory of dispersive transport in amorphous semiconductors. *J. Phys. Colloq.* **1981**, *42* (C4), C4-127-C4-131. https://doi.org/10.1051/jphyscol:1981424.

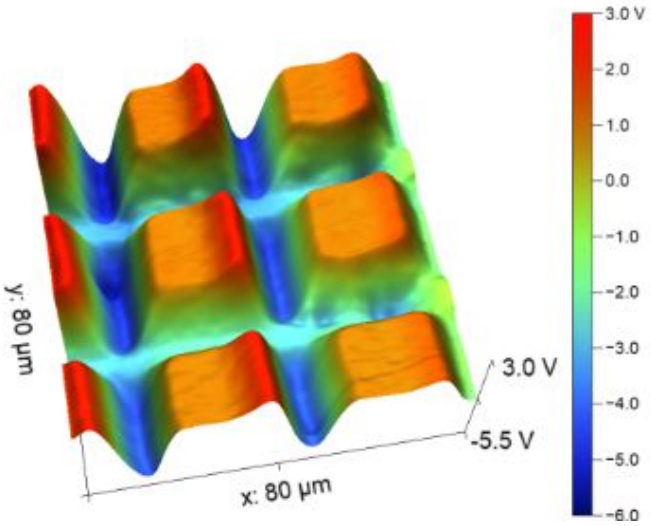
(51) Phillips, J. C. Stretched Exponential Relaxation in Molecular and Electronic Glasses. *Rep. Prog. Phys.* **1996**, *59* (9), 1133–1207. https://doi.org/10.1088/0034-4885/59/9/003.

(52) Shimakawa, K.; Inami, S.; Elliott, S. R. Reversible Photoinduced Change of Photoconductivity in Amorphous Chalcogenide Films. *Phys. Rev. B* **1990**, *42* (18), 11857–11861. https://doi.org/10.1103/PhysRevB.42.11857.

(53) Shoulders, W. T.; Novak, J.; Dussauze, M.; Musgraves, J. D.; Richardson, K. Thermal Poling Behavior and SHG Stability in Arsenic-Germanium Sulfide Glasses. *Opt. Mater. Express* **2013**, *3* (6), 700. https://doi.org/10.1364/OME.3.000700.

(54) Redkov, A. V.; Melehin, V. G.; Statcenko, V. V.; Lipovskii, A. A. Nanoprofiling of Alkali-Silicate Glasses by Thermal Poling. *J. Non-Cryst. Solids* **2015**, *409*, 166–169. https://doi.org/10.1016/j.jnoncrysol.2014.11.007.

TOC graphic


3.0 V
2.0
1.0
0.0
-1.0
-2.0
-3.0
-4.0
-5.0
-6.0
y: 80 µm
3.0 V
-5.5 V
x: 80 µm

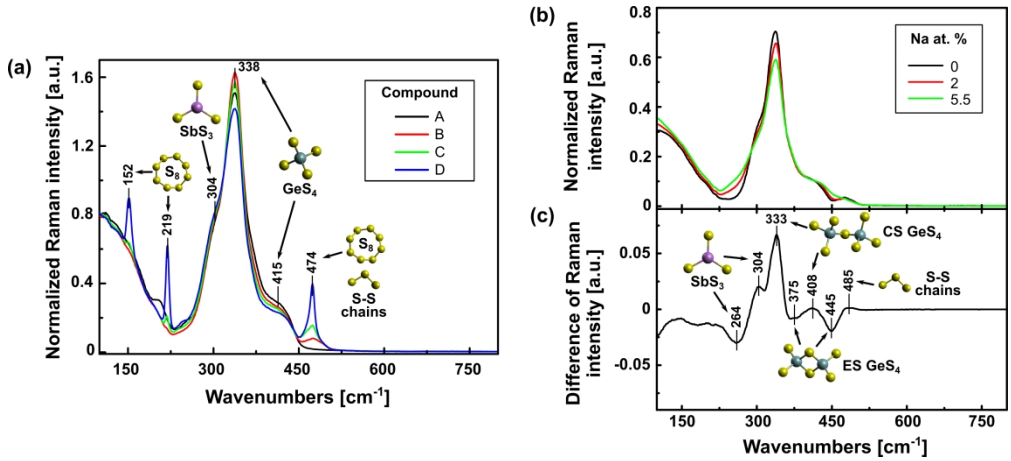


Figure 1. Raman spectra of the pristine ChG samples: (a) A, B, C and D glasses series with increasing S/Ge ratio, (b) Na0, Na2 and Na5.5 glasses series with increasing sodium content and constant ratio between the other components and (c) Raman difference spectra: response of Na5.5 subtracted to Na0 response.

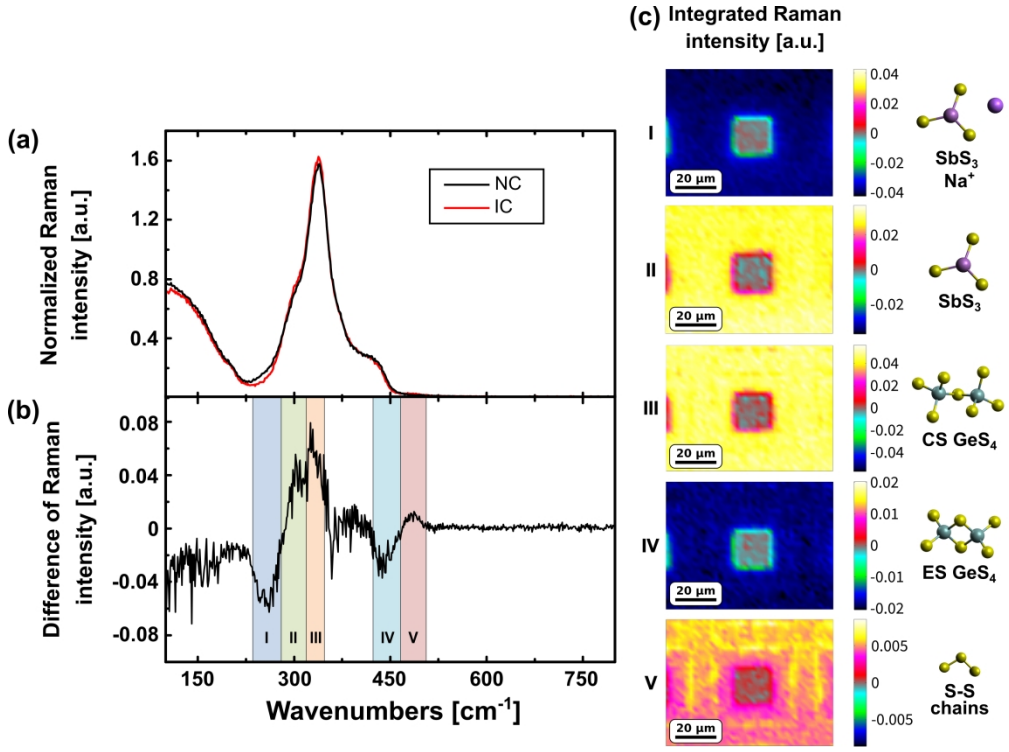


Figure 2. (a) Raman spectra from the thermally poled A glass, the black line corresponds to the region non in contact (NC) with the conductive zone and the red line in contact (IC). (b) Raman difference spectrum where the spectrum of the NC region has been subtracted to the IC region. (c) Spatial evolution of the Raman intensity of the different bands revealed by the Raman difference spectrum and the schematic representation of the glass units they are associated with.

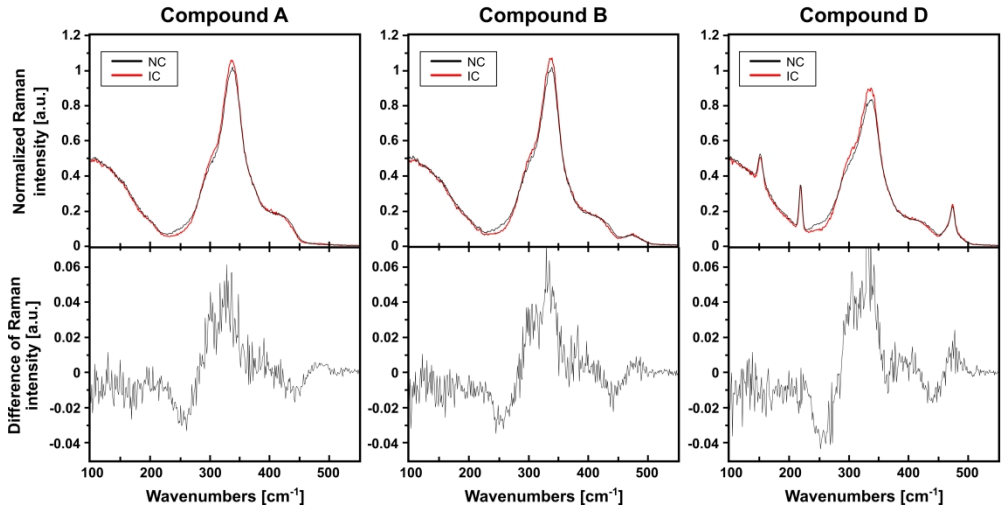


Figure 3. (Top) Raman spectra from the different thermally poled glasses A, B and D presenting different S/Ge ratio and same sodium content. The black lines correspond to the region not in contact (NC) with the conductive zone and the red line in contact (IC). (Bottom) Raman different spectra for each glass where the spectrum of the NC region has been subtracted from the spectrum of the IC region.

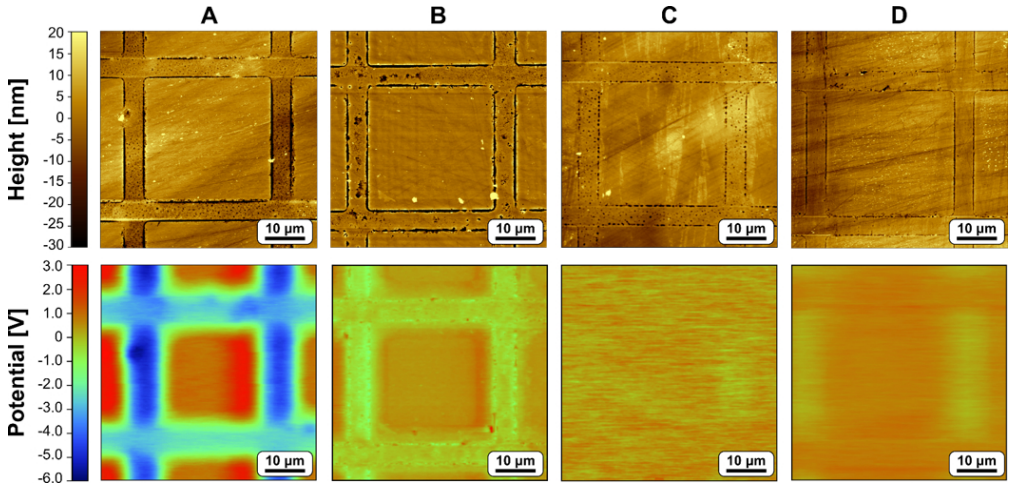


Figure 4. AFM measured topography (top) and KPFM measured surface potential (bottom) images of the post-poling surface of glasses A, B, C and D i.e. increasing sulfur content with fixed sodium content.

178x84mm (150 x 150 DPI)

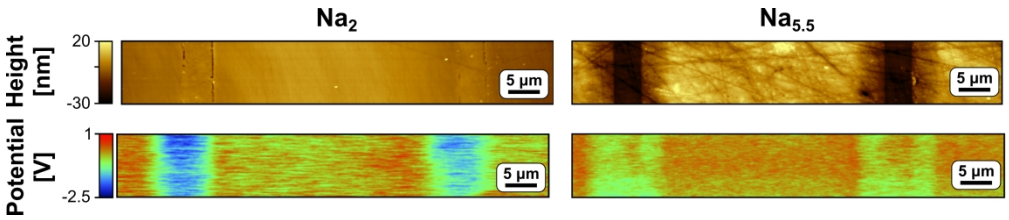


Figure 5. AFM measured topography (top) and KPFM measured surface potential (bottom) images of the post-poling surface of glasses Na2 and Na5.5 i.e. increasing sodium content with other component's ratios constant. The results obtained for Na0 (no sodium) are not presented as no effect – topology or potential – were observed in the absence of alkali cation in the initial composition.

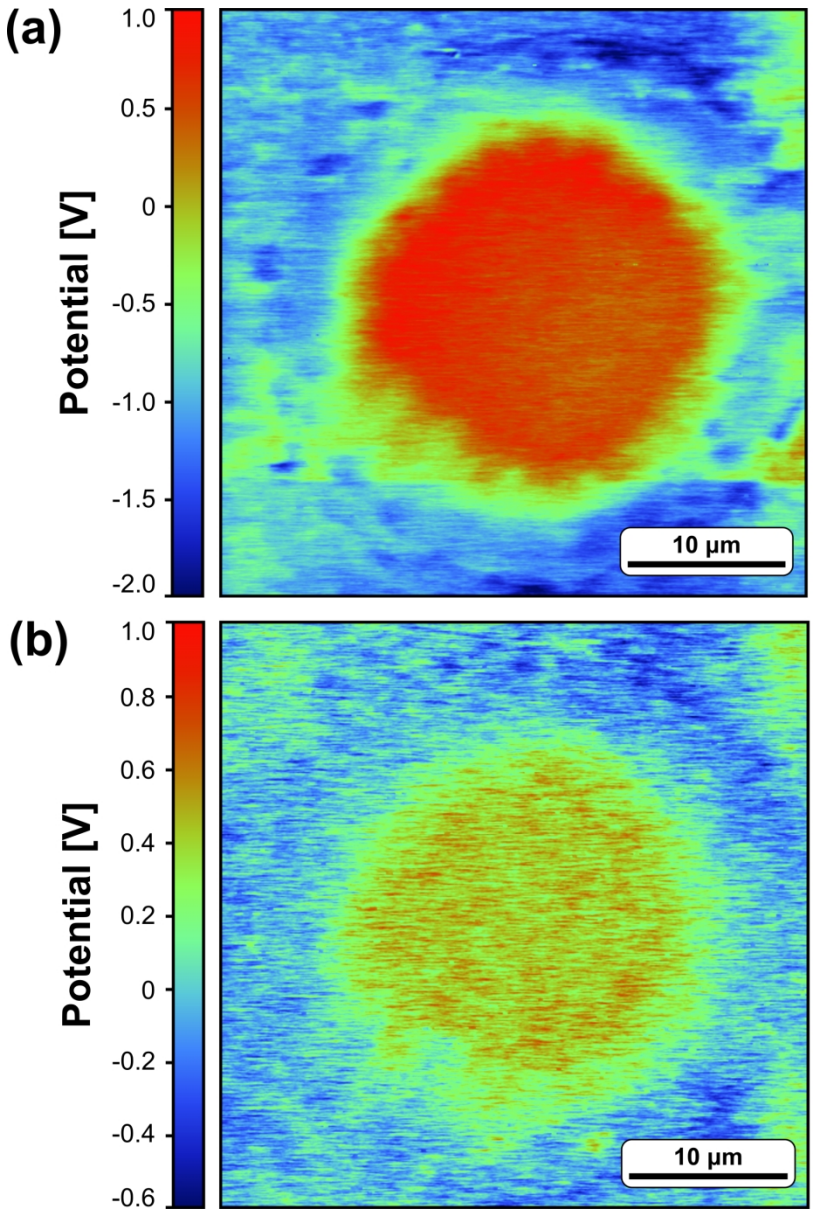


Figure 6. KPFM imaging of a thermally poled glass B using a disk pattern on the electrode measured just after the treatment (a) and after 24 months (b).